

Non-linear Analysis of Viscous Flow Around Cavitating Hydrofoils

S.A. Kinnas S. Mishima W.H. Brewer

Department of Ocean Engineering
Massachusetts Institute of Technology

Twentieth Symposium on Naval Hydrodynamics
University of California, Santa Barbara, CA
21-26 August 1994

ABSTRACT

The flow around partially or super-cavitating hydrofoils is treated with a viscous/inviscid interactive method. The inviscid cavity flow model is based on a fully non-linear boundary element method, in which the boundary conditions are applied on the exact cavity surface. The viscous flow model is based on boundary layer theory applied on the compound foil, consisting of the union of the cavity and hydrofoil surface. The friction coefficient is forced to zero everywhere on the cavity. The cavity detachment point is determined from a criterion applied on the viscous flow on the hydrofoil upstream of the cavity. The effect of Reynolds number on the predicted cavity extent and volume for given cavitation number is studied when the angle of attack is kept fixed or when the lift coefficient is kept fixed. Finally, the *equivalent* cavitation number is proposed as a way of including the effects of viscosity in three-dimensions.

1 INTRODUCTION

A general potential-based boundary element method has been developed for the non-linear analysis of the inviscid cavitating flow around hydrofoils or propeller blades. The flow around partially or super-cavitating hydrofoils in two or three dimensions was addressed first. For given cavity extent (length) [11] or cavitation number [13, 6], the cavity shape, not known a priori, was determined in an iterative manner until the dynamic and the kinematic boundary conditions were both satisfied on the cavity boundary. The most important finding in [11, 13] was the fact that the iterative process for finding the cavity surface was converging *much* quicker than in previously developed velocity-based boundary el-

ement methods. In particular, it was found that even the cavity solution from the first iteration, in which the cavity panels were located on the hydrofoil surface underneath the cavity, was *very close* to the fully non-linear converged solution. The method was finally extended to include the analysis of time-varying cavitating flows around propeller blades [12], [5].

The boundary element method has been found to be a computationally efficient, robust and versatile tool for the inviscid analysis of cavitating flows around arbitrary geometries in two or three dimensions. Nevertheless, the method has the following shortcomings: (a) it only treats the inviscid flow around the foil and cavity, (b) it treats the cavity detachment point as an input parameter, and (c) it assumes the cavity to be followed by a zero (or given) thickness wake.

In the present paper, a method is presented to take into account all of the above. The method couples the existing inviscid flow solution to a boundary layer solution [4]. It was first applied for the analysis of the fully wetted flow around hydrofoils [4] as well as propeller blades [8]. Initially, the method was applied on partially cavitating hydrofoils [19] by making the “thin” cavity assumption. Now the method is extended to treat the flow around partially cavitating hydrofoils in *fully non-linear* theory, as well as the flow around super-cavitating hydrofoils. The method is applied on several hydrofoil geometries and the effect of Reynolds number on the cavity solution is investigated. Finally, a way of incorporating the effects of viscosity in three dimensions, via the *equivalent* cavitation number is proposed.

- pressure condition at cavity termination:

$$|\mathbf{q}_{tr}| = U_\infty \sqrt{1 + \sigma} [1 - f(x)] \quad (9)$$

Where \mathbf{q}_{tr} is the velocity vector over a transition region of length λ at the end of the cavity and f is an algebraic function of the chordwise distance x [13]. This corresponds to a pressure recovery cavity termination model [15]. In the case of super-cavitating flows we apply the “end parabola” model [5], which is a variation of the Riabouchinsky “end plate” model.

- closure condition at the end of the cavity.
- Kutta condition at the foil trailing edge.

In solving equation (3), the wetted foil and cavity surface are discretized into N ($N \times M$ in 3-D) linear (quadrilateral in 3-D) panels. Initially, a double cosine spacing was employed over the cavity and the fully wetted part of the foil [11]. A new panel arrangement, called the “blended” spacing (see Appendix A for details), is being used in this work. In addition to being more versatile, the present arrangement has been found to improve the rate of convergence of the cavity solution as well as that of the calculated forces.

Over each panel, the source strength (proportional to $\partial\phi/\partial n$) and the dipole strength (proportional to ϕ) are assumed to be constant. The potential jump in the wake, $\Delta\phi_W$, is taken to be equal to the difference of the potentials at the trailing edge panels on the same strip [16]. On each panel representing the fully wetted foil, the source strengths are known and given by equation (6) but the dipole strengths are unknown. On each panel representing the cavity, the dipole strengths are known and given by equations (7) or (9) but the source strengths are unknown. The unknown dipole or source strengths are determined by applying equation (3) on all panels and by inverting the resulting system of linear equations.

In applying the conditions mentioned previously, the surface of the cavity must be known. The procedure for determining the location of the cavity surface is given next:

In two-dimensions

The cavity surface is defined by the location of the cavity detachment point l_D , the location of the cavity end point l (also defined as the cavity length), and the cavity ordinates between these

points. As already mentioned in the introduction, the location of the cavity detachment is assumed to be known in the inviscid cavity model. Thus the two-dimensional cavitating hydrofoil analysis can be formulated in terms of the following problems:

- For given l and l_D find the corresponding σ
- For given σ and l_D find l

In both these problems, described in detail in [11] and [13], the cavity shape is determined in an iterative manner. In brief, the cavity surface is updated until the kinematic boundary condition is satisfied on the cavity (in addition to the dynamic condition mentioned earlier):

$$\mathbf{q}_c \cdot \mathbf{n} = 0 \quad ; \quad \text{on the cavity} \quad (10)$$

The first iteration for the cavity shape is taken to be:

- the foil surface under the cavity, for partially cavitating hydrofoils
- the cavity shape from linear theory, for super-cavitating hydrofoils

The iterative process has been found to converge quickly to the final cavity shape [11], [13]. In particular, even the first iteration has been found to produce a cavity shape which is remarkably close to the converged *fully non-linear* cavity shape.

In three-dimensions

The characteristics of the method in three-dimensions may be summarized as follows:

- It only carries the first iteration, thus utilizing the same panelling to that of fully wetted flows.
- It finds the cavity planform for *given* cavitation number and for given cavity detachment in an iterative manner, until the thickness of the cavity at its trailing edge is equal to zero everywhere along the span.
- It includes, in an iterative manner, the cross-flow terms in applying equation (7).
- It is able to handle arbitrary cavity planforms on a *fixed* grid. This became possible with the introduction of the *split panel technique* [13]. This technique enabled us to treat panels which were intersected by the trailing



Figure 3: Non-cavitating hydrofoil with its boundary layer displacement thickness.

edge of the cavity as *one*, rather than two parts (i.e. the cavitating and the fully wetted part).

- It utilizes a *unified* formulation and numerical implementation for partial cavitation, super-cavitation, as well as mixed partial/super-cavitation [6].

3 VISCOUS FULLY-WETTED FLOW MODEL

3.1 Boundary Layer Equations

Consider a non-cavitating 2-D hydrofoil in uniform inflow \mathbf{U}_∞ , as shown in Figure 3. The viscous flow is assumed to be confined within a thin boundary layer on the foil and wake surface. The effect of viscosity on the inviscid flow is accounted via the “blowing sources”, $\hat{\sigma}$, which are defined as:

$$\hat{\sigma} = \frac{d(U_e \delta^*)}{ds} \quad (11)$$

where U_e is the velocity at the “edge” of the boundary layer, δ^* is the displacement thickness and s is the arc-length along the foil or wake surface. For given U_e distribution, the boundary layer parameters are determined from the following equations [20], [17], [4]:

1. The momentum integral equation:

$$\frac{d\theta}{ds} + (2 + H) \frac{\theta}{U_e} \frac{dU_e}{ds} = \frac{C_f}{2} \quad (12)$$

where θ is the momentum thickness, $H = \delta^*/\theta$ is the momentum shape factor, and C_f is the friction coefficient. In the wake of the foil the following condition is enforced:

$$C_f = 0 ; \quad \text{in the wake} \quad (13)$$

2. The kinetic energy integral equation:

$$\begin{aligned} \theta \frac{dH^*}{ds} + [2H^{**} + H^*(1 - H)] \frac{\theta}{U_e} \frac{dU_e}{ds} \\ = 2C_D - H^* \frac{C_f}{2} \end{aligned} \quad (14)$$

3. A third equation which is different for laminar or turbulent flow:

- for laminar flow:

$$\frac{d\tilde{n}}{ds} = \frac{d\tilde{n}}{dRe_\theta} \frac{dRe_\theta}{ds} \quad (15)$$

where \tilde{n} is the amplitude of the most amplified Tollmien-Schlichting wave.

- for turbulent flow:

$$\begin{aligned} \frac{\delta}{C_\tau} \frac{dC_\tau}{ds} = 5.6 \left[C_{\tau_{EQ}}^{1/2} - C_\tau^{1/2} \right] + 2\delta \times \\ \left\{ \frac{4}{3\delta^*} \left[\frac{C_f}{2} - \left(\frac{H_k - 1}{6.7H_k} \right)^2 \right] - \frac{1}{U_e} \frac{dU_e}{ds} \right\} \end{aligned} \quad (16)$$

where C_τ is the maximum shear stress coefficient.

The variables H^* , H^{**} , C_D , $C_{\tau_{EQ}}$, H_k and Re_θ are defined in [4]. The necessary number of equations which interrelate these variables among themselves as well as with the unknowns are also given in [4].

In laminar flow, equations (12), (14) and (15) are solved with respect to the three unknowns: δ^* , θ and \tilde{n} . In turbulent flow, equations (12), (14) and (16) are solved with respect to the unknowns: δ^* , θ and C_τ . The transition from laminar to turbulent flow is defined when \tilde{n} becomes equal to a specified critical value: \tilde{n}_{crit} . The option for specifying the transition point on either side of the hydrofoil is also available.

3.2 Viscous/Inviscid Flow Coupling

The presence of the blowing sources will modify Green’s formula, equation (3), when applied on the foil surface, as follows ²:

$$\begin{aligned} \frac{\phi^v}{2} = \int_S \left[G(-\mathbf{U}_\infty \cdot \mathbf{n}) ds - \phi^v \frac{\partial G}{\partial n} \right] ds - \\ - \int_W \Delta \phi_W^v \frac{\partial G}{\partial n} ds + \int_{S_{UW}} \hat{\sigma} G ds \end{aligned} \quad (17)$$

²A discretized version of this equation was first given in [8].

where ϕ^v is the perturbation potential along the foil surface, modified due to viscous effects. Notice that the blowing sources are placed *on* the foil surface. ϕ^v satisfies the following (kinematic) boundary condition on the foil:

$$\frac{\partial \phi^v}{\partial n} = -\mathbf{U}_\infty \cdot \mathbf{n} + \hat{\sigma} \quad (18)$$

Equation (17) may be written in the following compact form:

$$\mathcal{A}\phi^v = \mathcal{B}\{-\mathbf{U}_\infty \cdot \mathbf{n}\} + \mathcal{C}\hat{\sigma} \quad (19)$$

where the linear operators \mathcal{A} , \mathcal{B} and \mathcal{C} are defined as:

$$\mathcal{A}\{f\} = \frac{f}{2} + \int_S f \frac{\partial G}{\partial n} ds + \int_W \Delta f_W \frac{\partial G}{\partial n} ds \quad (20)$$

$$\mathcal{B}\{f\} = \int_S f G ds \quad (21)$$

$$\mathcal{C}\{g\} = \int_{S \cup W} g G ds \quad (22)$$

with f being a continuous function of the arc-length along the foil surface and g being a continuous function of the arc-length along the foil and wake surface. Δf_W is equal to the jump in f at the foil trailing edge, between the pressure and suction side.

The perturbation potential ϕ^v may be found from inverting equation (19):

$$\phi^v = \mathcal{A}^{-1} \circ \mathcal{B}\{-\mathbf{U}_\infty \cdot \mathbf{n}\} + \mathcal{A}^{-1} \circ \mathcal{C}\{\hat{\sigma}\} \quad (23)$$

where \mathcal{A}^{-1} is the inverse operator of \mathcal{A} . Equation (23) may also be written as:

$$\phi^v = \phi^{inv} + \mathcal{A}^{-1} \circ \mathcal{C}\{\hat{\sigma}\} \quad (24)$$

where ϕ^{inv} is the perturbation potential in inviscid flow, given from:

$$\phi^{inv} = \mathcal{A}^{-1} \circ \mathcal{B}\{-\mathbf{U}_\infty \cdot \mathbf{n}\} \quad (25)$$

The magnitude of the total velocity at the edge of the boundary layer, U_e , can then be determined from:

$$U_e = \mathbf{U}_\infty \cdot \mathbf{s} + \frac{\partial \phi^v}{\partial s} = U_e^{inv} + \mathcal{D}\{\hat{\sigma}\} \quad (26)$$

with \mathbf{s} being the unit vector tangent to the foil or wake surface. U_e^{inv} is the magnitude of the total velocity on the foil or wake surface in *inviscid* flow:

$$U_e^{inv} = \mathbf{U}_\infty \cdot \mathbf{s} + \frac{\partial \phi^{inv}}{\partial s} \quad (27)$$

The operator \mathcal{D} is defined as:

$$\mathcal{D} = \left[\frac{d}{ds} \right] \circ \mathcal{A}^{-1} \circ \mathcal{C} \quad (28)$$

Using equation (11), equation (26) may be written as:

$$U_e = U_e^{inv} + \mathcal{D} \left\{ \frac{d(U_e \delta^*)}{ds} \right\} \quad (29)$$

or

$$U_e = U_e^{inv} + \mathcal{E}\{U_e \delta^*\} \quad (30)$$

with the operator \mathcal{E} defined as:

$$\mathcal{E} = \mathcal{D} \circ \left[\frac{d}{ds} \right] \quad (31)$$

Equation (30) provides the actual mechanism for coupling the viscous with the inviscid solution. This equation must be solved together with the boundary layer equations (12), (14) and (15) or (16). The boundary layer equations are solved first, with $U_e = U_e^{inv}$, and the δ^* distribution on the foil and its wake is determined. Equation (30) is then solved with respect to U_e . The updated U_e is then used in solving the boundary layer equations once more. This process is repeated until convergence of the solution.

In solving the previously mentioned equations, the foil and its wake are discretized with N and N_W linear panels, respectively. The boundary layer variables δ^* , θ , C_τ (or \tilde{n}), and the edge velocity U_e are defined at the edges of each panel. Green's formula, equation (17), is discretized by assuming constant source and dipole distributions over each panel [9, 14]. The blowing source, $\hat{\sigma}$, on each panel is also assumed to be constant with its value given from [8]:

$$\hat{\sigma} = \frac{\Delta m}{\Delta s} \quad (32)$$

with m defined as the mass defect: $m = U_e \delta^*$. Δm is the difference between the m 's at the edge of the panel and Δs is the arc-length of the foil between the edges of the panel.

The operators \mathcal{A} , \mathcal{B} and \mathcal{C} are discretized into the influence coefficient matrices with dimensions $N \times N$, $N \times N$ and $N \times N + N_W$, respectively [8]. The operator $[d/ds]$ is discretized into $[\Delta/\Delta s]$.



Figure 4: Partially cavitating hydrofoil with its boundary layer displacement thickness.

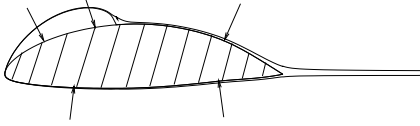


Figure 5: Hydrofoil and cavity surface on which inviscid and boundary layer flow equations are applied - “Thin” cavity approach.

4 VISCOUS CAVITY MODEL

4.1 Partially Cavitating Hydrofoil

Consider now a partially cavitating hydrofoil in viscous flow, as shown in Figure 4. The viscous flow in the vicinity of the cavity is assumed to be confined to a thin boundary layer. The two-phase flow in the vicinity of the cavity is ignored, and the fluid/vapor interface is treated as a constant pressure free-streamline. We present two approaches of formulating the viscous cavity model.

“Thin” cavity approach

In this case both the cavity and the boundary layer thickness are assumed to be “small”. The panels representing the cavity are assumed to be located on the foil surface underneath the cavity, as shown in Figure 5. This is implemented in [19] by defining the cavity sources $\hat{\sigma}^c$ as follows:

$$\hat{\sigma}^c = \frac{d(U_e h)}{ds} \quad (33)$$

with h being the cavity thickness, defined normal to the foil surface. Notice the similarity of equation (33) with equation (11). The effects of cavity thickness are thus readily incorporated into equation (30) as follows:

$$U_e = U_e^{inv} + \mathcal{E}\{U_e \delta^* + U_e h\} \quad (34)$$

In other words, equation (34) makes no distinction between the cavity and the displacement thickness.

The dynamic boundary condition, equation (7), is implemented by requiring:

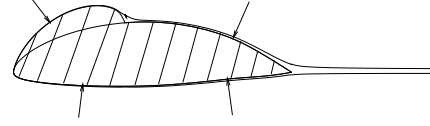


Figure 6: Hydrofoil and cavity surface on which inviscid and boundary layer flow equations are applied - Non-linear cavity approach.

$$U_e = U_\infty \sqrt{1 + \sigma} ; \text{ on the cavity} \quad (35)$$

The boundary layer equations are now solved together with equations (34) and (35). It is assumed that *no* frictional forces can be sustained at the interface between the fluid and the vapor, i.e:

$$C_f = 0 ; \text{ on the cavity} \quad (36)$$

A cavity termination model, similar to that described in Section 1, is applied. Cavity closure ($h = 0$) is imposed at the cavity trailing edge. An iterative algorithm (based on Newton-Raphson method) for solving the boundary layer and the cavity equations, is given in [19].

Non-linear cavity approach

In this case the cavity thickness is not assumed to be “small” compared to the foil thickness. The boundary layer displacement thickness though, is still assumed to be “small”. The boundary conditions are now applied on the “non-linear” cavity and foil surface, shown in Figure 6. The “non-linear” cavity shape has resulted from the inviscid non-linear cavity theory, described in Section 2. The boundary layer equations now are integrated along the non-linear cavity and foil surface.

Equation (30) will now be modified to:

$$U_e^{NL} = U_e^{inv,NL} + \mathcal{E}^{NL}\{U_e^{NL} \delta^*\} \quad (37)$$

where the superscript NL corresponds to the “compound” foil, defined from the union of the original foil and the non-linear cavity surface. The velocity on the cavity will be given as:

$$U_e^{inv,NL} = U_\infty \sqrt{1 + \sigma^{inv}} \quad (38)$$

where σ^{inv} is the cavitation number resulting from non-linear inviscid cavity theory, for given l_D and l .

$\tau/c=0.05$, NACA66
$f_0/c=0.02$, NACA $a=0.8$
$\alpha=3\text{deg}$

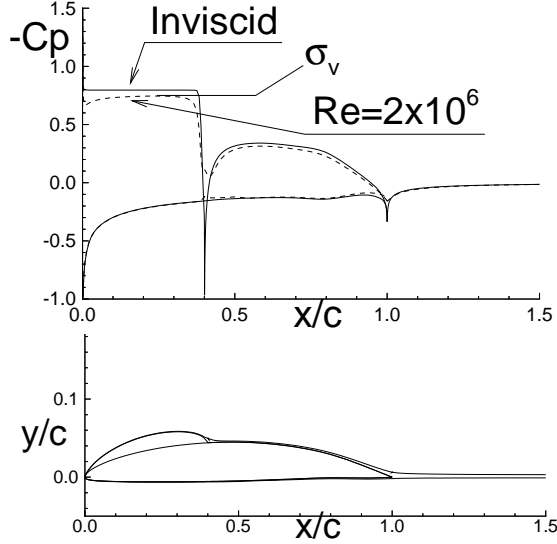


Figure 7: Pressure distribution on foil and cavity resulting from inviscid and viscous solution. The cavity resulting from inviscid *non-linear* model and the corresponding boundary layer displacement thickness are also shown. Definition of “viscous” cavitation number, σ_v .

Applying the boundary layer equations on the compound foil, with $C_f = 0$ on the cavity, will result in the displacement thickness and pressure³ distributions, shown in Figure 7⁴. It may be seen on this figure that the assumption of “small” displacement thickness is still valid. Notice that the “viscous” $-C_p$ distribution on the cavity is lower than the inviscid (for which $-C_p = \sigma^{inv}$). Also notice that the viscous solution has perturbed “somewhat” the dynamic boundary condition, which requires the pressure distribution to be constant on the cavity. We define the cavitation number in the presence of viscosity (for l_D and l fixed) from:

$$\sigma^v = \max[-C_p^v] \quad (39)$$

where C_p^v is the pressure coefficient in the presence

³The pressure coefficient C_p is defined as: $C_p = 2(p - p_\infty)/(\rho U_\infty^2)$.

⁴The Reynolds number Re is defined as: $Re = \frac{U_\infty c}{\nu}$

of viscosity. This definition is also shown in Figure 7.

Even though the viscous pressure distribution shown in Figure 7 is “nearly” constant, it is still desired to “estimate” the error in cavitation number and cavity shape by ignoring the variation in pressure along the cavity. This is accomplished as follows:

If ϕ^{cor} is the “correct” perturbation potential which satisfies the “exact” dynamic boundary condition in viscous flow, equation (8), on the cavity, then :

$$\frac{\partial \phi^{cor}}{\partial s} + \mathbf{U}_\infty \cdot \mathbf{s}^{NL} = U_\infty \sqrt{1 + \sigma^{cor}} \quad (40)$$

where the superscript “*cor*” corresponds to the “correct” solution, defined in the previous paragraph.

On the wetted foil, the following condition will be satisfied:

$$\frac{\partial \phi^{cor}}{\partial n} = -\mathbf{U}_\infty \cdot \mathbf{n} + \hat{\sigma}^{NL} \quad (41)$$

Equations (40) and (41) take the same form as equations (8) and (6) by adding the blowing source $\hat{\sigma}^{NL}$ to $-\mathbf{U}_\infty \cdot \mathbf{n}$. We thus treat the “correction” problem as a cavity problem (applied on the compound foil)⁵ and determine ϕ^{cor} and σ^{cor} . The new value of $\partial \phi^{cor}/\partial n$ on the cavity is also determined. The cavity shape then needs to be corrected by h^{cor} , defined normal to the original cavity shape. If \mathbf{n}^{cor} is the unit vector normal to the correct cavity shape, the following kinematic boundary condition must be satisfied:

$$[\nabla \phi^{cor} + \mathbf{U}_\infty] \cdot \mathbf{n}^{cor} = \hat{\sigma}^{NL} ; \text{ on the cavity} \quad (42)$$

The normal vector, to first order in h^{cor} , will be given from [11]:

$$\mathbf{n}^{cor} = \mathbf{n}^{NL} - \frac{dh^{cor}}{ds} \mathbf{s}^{NL} \quad (43)$$

Combining equations (42) and (43) gives the following differential equation for h^{cor} :

$$U_\infty \sqrt{1 + \sigma^{cor}} [1 - f(x)] \frac{dh^{cor}}{ds} = \frac{\partial \phi^{cor}}{\partial n} + \mathbf{U}_\infty \cdot \mathbf{n}^{NL} - \hat{\sigma}^{NL} \quad (44)$$

⁵The effect of the blowing sources in the wake needs also to be included in the right-hand side of the resulting equations.

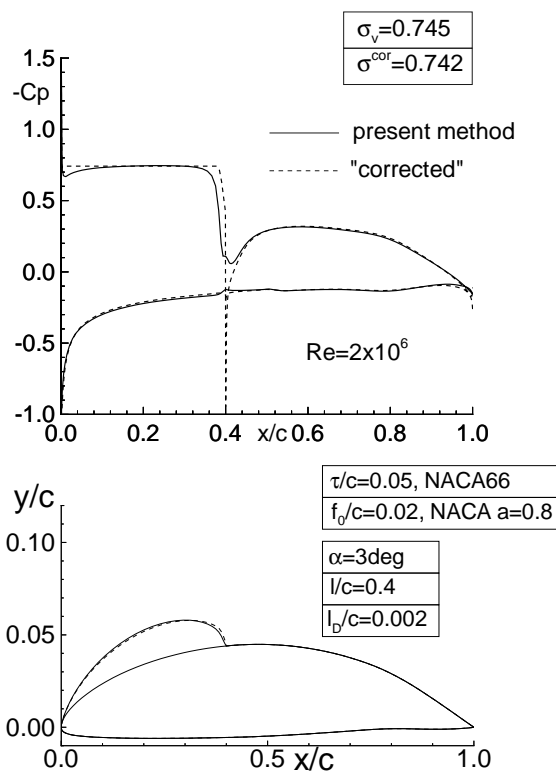


Figure 8: Non-linear cavity shape resulting from present method and “corrected” to satisfy the “exact” dynamic boundary condition. The corresponding pressure distributions are also shown.

Integrating equation (44) we find h^{cor} and the “correct” cavity shape given on Figure 8. The “correct” cavity pressure distribution is also given. Comparing the “correct” to the original cavity shape and cavitation number, we notice that the error is relatively small. This correction will be omitted from all subsequent results.

Cavity shapes, predicted by the present “non-linear” and the “thin” cavity formulation, for given cavitation number, are shown in Figures 9 and 10. As expected the results from the two methods are close to each other for cavities which are indeed thin when compared to the foil thickness. For cavities whose thickness is of the same order as the foil thickness, the “thin” cavity method overpredicts the cavity shape extent and size appreciably, as shown in Figure 10.

Cavity detachment

It is well known that the location of the cavity detachment point may affect (sometimes substantially) the predicted cavity extent and volume. Detaching the cavity at the leading edge of a round nose hydrofoil may often lead to non-

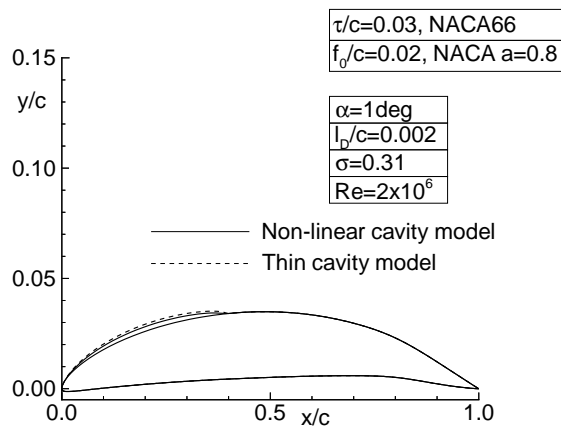


Figure 9: Cavity shapes predicted from thin and non-linear (present) cavity viscous models, for given cavitation number. Foil geometry and flow conditions produce a thin cavity in comparison to the foil thickness.

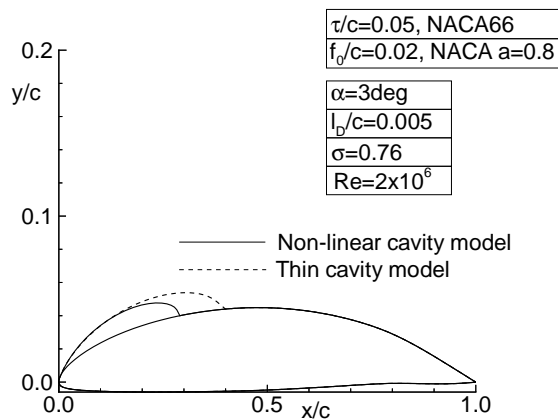


Figure 10: Cavity shapes predicted from thin and non-linear (present) cavity viscous models, for given cavitation number. Foil geometry and flow conditions produce a cavity with thickness which is comparable to the foil thickness.

physical solutions, i.e. cavities which intersect the foil. One such case is shown in Figure 11. The *smooth detachment* condition ⁶[18, 3] requires the slope and the curvature of the cavity at detachment to be equal to that of the foil. This condition ensures that the cavity does not intersect the foil at the leading edge and, at the same time, that the pressures on the wetted foil, upstream of the cavity, are *larger* than the cavity pressure. This condition is equivalent to requiring the slope of the pressure distribution with respect to the foil arc-length at the cavity leading edge to be equal to zero [2, 10]. Such a case is shown in Figure 12. The smooth detachment point (SDP) in this case was determined by applying the inviscid cavity model and by varying l_D until the resulting pressure distribution had a zero slope at the leading edge of the cavity. Detaching the cavity upstream of the SDP will produce a cavity which intersects the foil. Detaching the cavity downstream of the SDP will produce pressures upstream of the cavity which are smaller than cavity pressure. However, it is widely known that in reality the cavity detachment is well downstream of the SDP. In addition, pressures *smaller* than the cavity pressure have been measured on the wetted flow upstream of the cavity detachment. A semi-empirical cavity detachment criterion for cavitating headforms was introduced by Arakeri [1]. This criterion was later extended by Franc & Michel [7] in the case of cavitating hydrofoils. In brief, they found that for hydrofoils, the cavity detachment occurs immediately downstream of a laminar separation point (LSP). Laminar separation occurs when $H = \delta^*/\theta = 4$ [20]. We thus apply the present viscous method for different detachment points until the boundary layer calculation shows laminar separation just ahead of the cavity leading edge. The pressure distribution for cavity detachment at laminar separation is shown on Figure 13. Finally, the effect of the cavity detachment point on the solution is shown on Figures 14 and 15. The importance of having the “right” cavity detachment point on the cavity prediction is apparent from these figures.

Sensitivity of cavity model on λ , N

The numerics of the inviscid cavity model have been validated extensively in [11] and [13]. The numerics of the viscous fully wetted model have been validated in [8]. In this work, the sensitivity of the results from applying the present combined inviscid/viscous cavity flow model is

⁶ Also called the Villat-Brillouin condition.

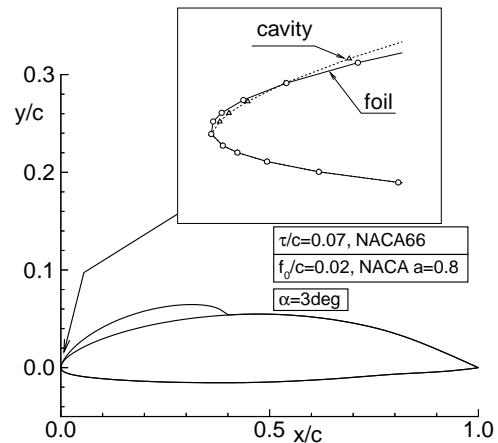


Figure 11: Cavity and foil surface at the leading edge. Cavity detachment at the LE.

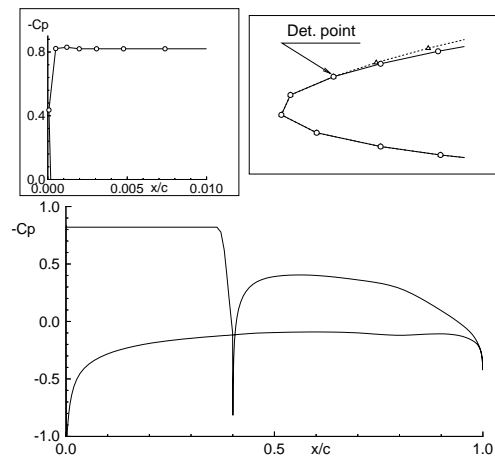


Figure 12: Pressure distribution on the foil and cavity. Smooth cavity detachment ($l_D = 0.0012$).

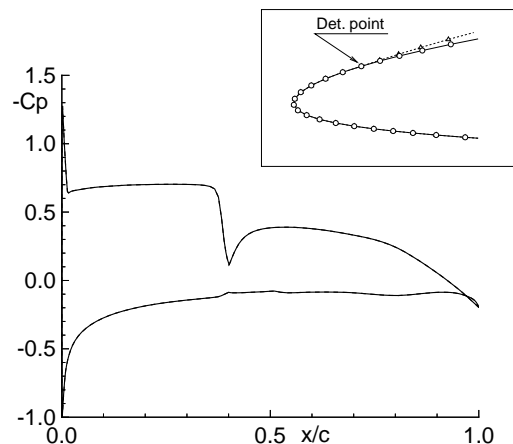


Figure 13: Pressure distribution on the foil and cavity. Cavity detachment set at laminar separation point ($l_D = 0.01$).

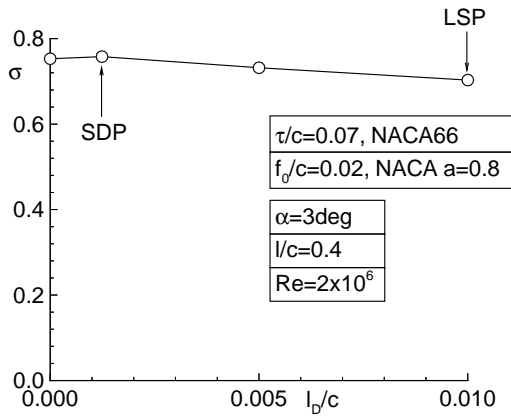


Figure 14: Effect of cavity detachment point on cavitation number.

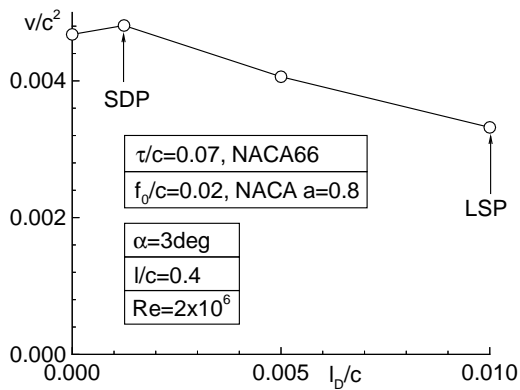


Figure 15: Effect of cavity detachment point on cavity volume.

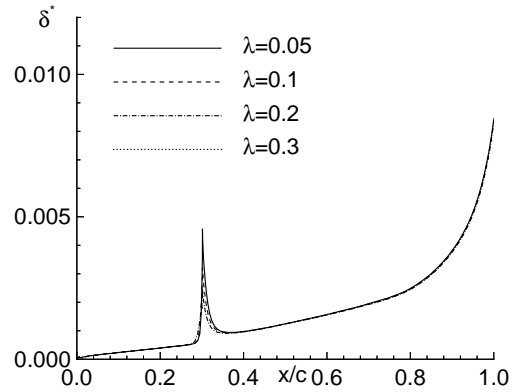


Figure 16: Effect of λ on boundary layer displacement thickness distribution.

studied. In Figure 16, the effect of the length of the cavity termination model λ on the predicted δ^* distribution on the suction side of the foil and cavity is shown. Notice that the predicted δ^* is practically the same everywhere on the cavity and foil, except in the vicinity of the cavity trailing edge. The effect of λ on the predicted solution is also shown on Table 1. It is again evident from this table that the results are practically independent of λ . This is a very fortunate characteristic of our method, since otherwise we would have to somehow determine λ from theory and/or experiment.

Finally, the convergence of the viscous cavity solution with number of panels N is given on Table 2.

Results

Results from applying the present method on partially cavitating hydrofoils are presented in this section. The hydrofoils consist of combinations of modified *NACA66* thickness form and *NACA a = 0.8* camber form. The viscous calculations are performed for $Re = 2 \times 10^6$ and $Re = 2 \times 10^7$ which are representative Reynolds numbers for model and full-scale marine propeller applications, respectively. Figures 17 and 18 show the cavity length and volume versus cavity cavitation number, in inviscid and viscous flow. Notice that the cavity extent and size decrease substantially with decreasing Re . The cavity shapes for $\sigma = 1$ are shown in Figure 19. Notice the reduction in the lift coefficient, C_L , with decreasing Re . This reduction reflects the change in the pressure distribution, shown in Figure 7.

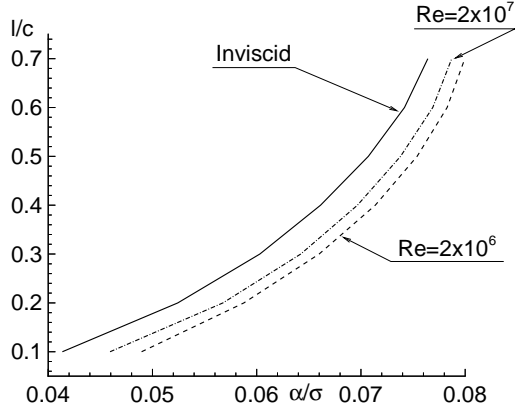


Figure 17: Cavity length versus cavitation number. Predicted by the inviscid and the present viscous method for two Reynolds numbers; $\tau/c = 0.04$, $f_o/c = 0.02$, $\alpha = 4^\circ$.

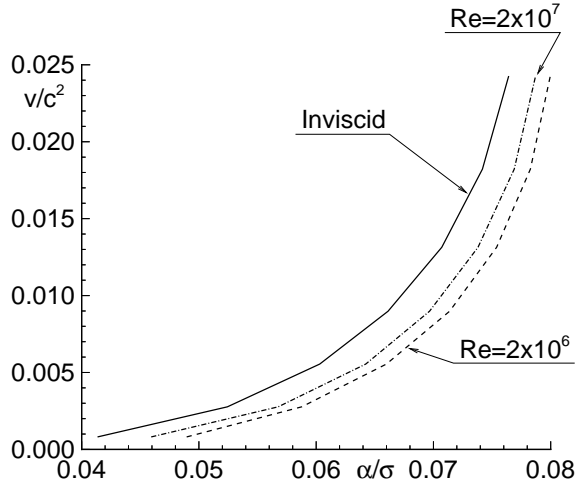


Figure 18: Cavity volume versus cavitation number. Predicted by the inviscid and the present viscous method for two Reynolds numbers; $\tau/c = 0.04$, $f_o/c = 0.02$, $\alpha = 4^\circ$.

λ	σ	V/c^2	C_L	C_D
0.05	0.754	0.00247	0.558	0.0119
0.1	0.755	0.00244	0.560	0.0119
0.2	0.758	0.00238	0.561	0.0118
0.3	0.761	0.00231	0.561	0.0118

Table 1: Effect of λ on viscous cavity solution: σ , V/c^2 , C_L and C_D ; $l/c = 0.3$, $NACA66(\tau/c = 0.07)$, $NACAa = 0.8(f/c = 0.02)$, $\alpha = 3^\circ$, $Re = 2 \times 10^6$, $N = 200$

N	σ	V/c^2	C_L	C_D
100	0.776	0.00250	0.566	0.0113
150	0.767	0.00245	0.564	0.0118
200	0.755	0.00244	0.560	0.0119

Table 2: Convergence of viscous cavity solution (σ , V/c^2 , C_L and C_D) with number of panels. Partially cavitating hydrofoil; same foil geometry as in Table 1.

Another way of showing the effect of Re on cavity extent and size is by keeping the cavitation number as well as the lift coefficient constant. In this way, a direct comparison of the predicted cavity length and volume in inviscid or viscous flow for given flow conditions (σ) and design requirements (lift coefficient, C_L , or thrust coefficient in the case of propellers) can be made. In Figures 20, 21, 22 and, 23, contour plots of constant σ and C_L are drawn on the l/c vs. α and V/c^2 vs. α space. In this manner, someone can look at the crossings of the same values of σ and C_L for different Re .

The corresponding cavity lengths and volumes as well as the angle of attack (required to produce the same lift) can be found and compared for different Re . From these contour plots, it may be seen that the cavity volume and length *decrease* with decreasing Re for fixed σ and C_L . This is the reverse trend from that shown in Figures 17 and 18 where the cavity volume and length *increase* with decreasing Re for fixed σ and α . The predicted cavity shapes with fixed σ and C_L and for different Re are shown in Figure 24.

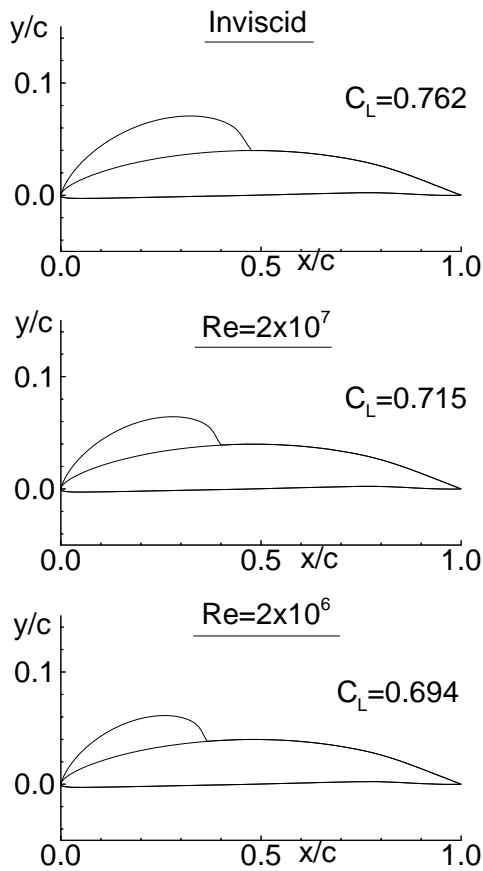


Figure 19: Cavity shapes predicted by the inviscid and the present viscous method for two Reynolds numbers. All hydrofoil sections are at $\alpha = 4^\circ$ and $\sigma = 1.0$. The corresponding lift coefficients are shown next to each foil; $\tau/c = 0.04$, $f_o/c = 0.02$.

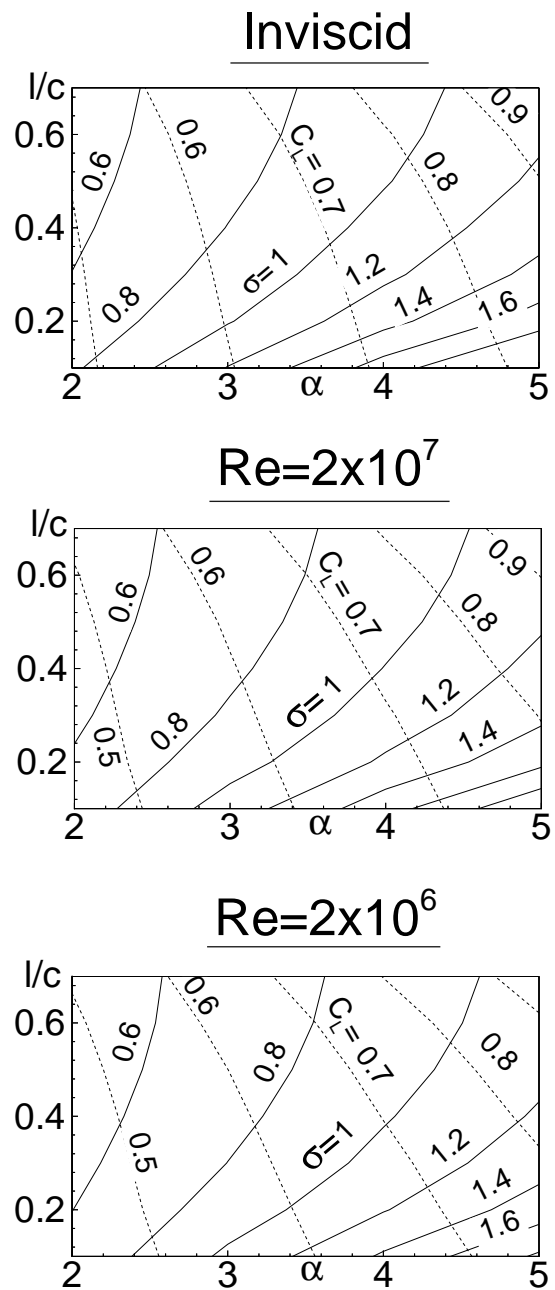


Figure 20: Contour plots of constant lift coefficient and cavitation number versus cavity length and angle of attack. Predicted by the present method for inviscid flow (top), $Re = 2 \times 10^7$ (middle) and $Re = 2 \times 10^6$ (bottom); $NACA66(\tau/c = 0.04)$, $NACA a = 0.8(f_o/c = 0.02)$.

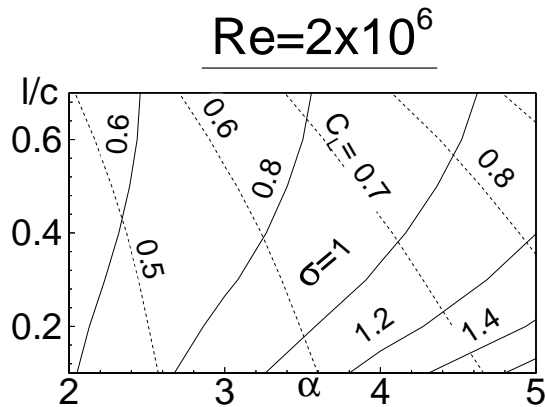
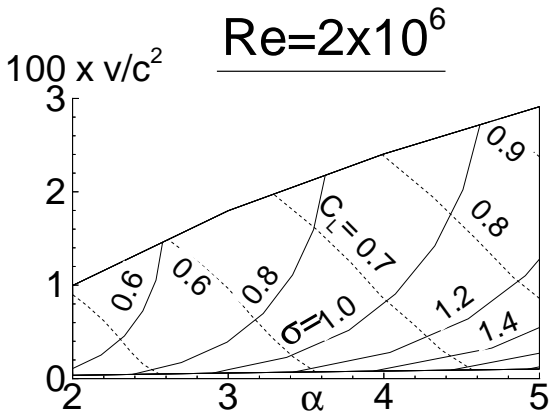
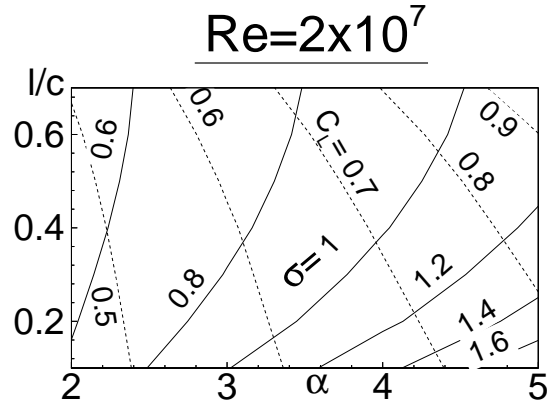
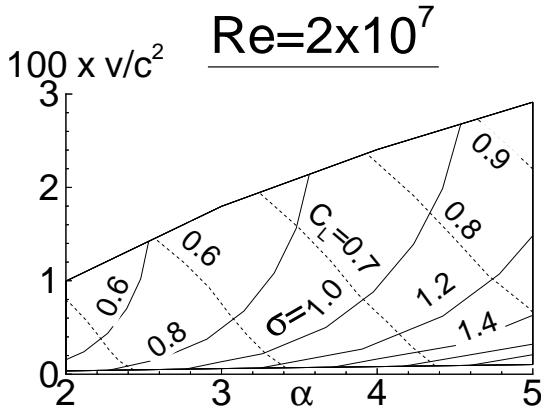
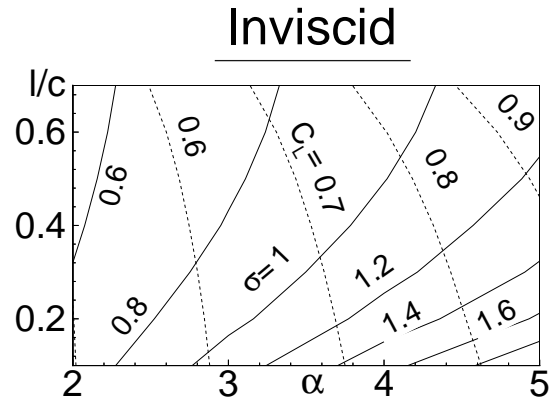
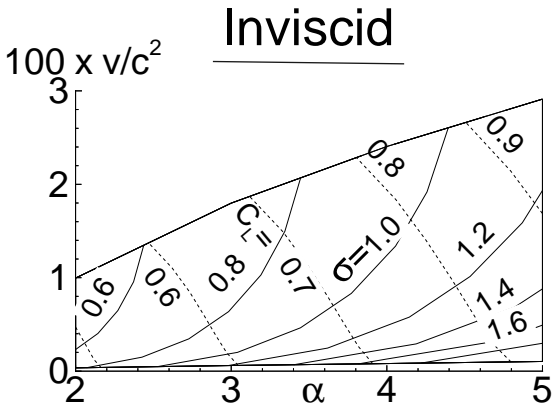


Figure 21: Contour plots of constant lift coefficient and cavitation number versus cavity volume and angle of attack. Predicted by the present method for inviscid flow (top), $Re = 2 \times 10^7$ (middle) and $Re = 2 \times 10^6$ (bottom); $NACA66(\tau/c = 0.04)$, $NACA a = 0.8(f_o/c = 0.02)$.

Figure 22: Contour plots of constant lift coefficient and cavitation number versus cavity length and angle of attack. Predicted by the present method for inviscid flow (top), $Re = 2 \times 10^7$ (middle) and $Re = 2 \times 10^6$ (bottom); $NACA66(\tau/c = 0.07)$, $NACA a = 0.8(f_o/c = 0.02)$.

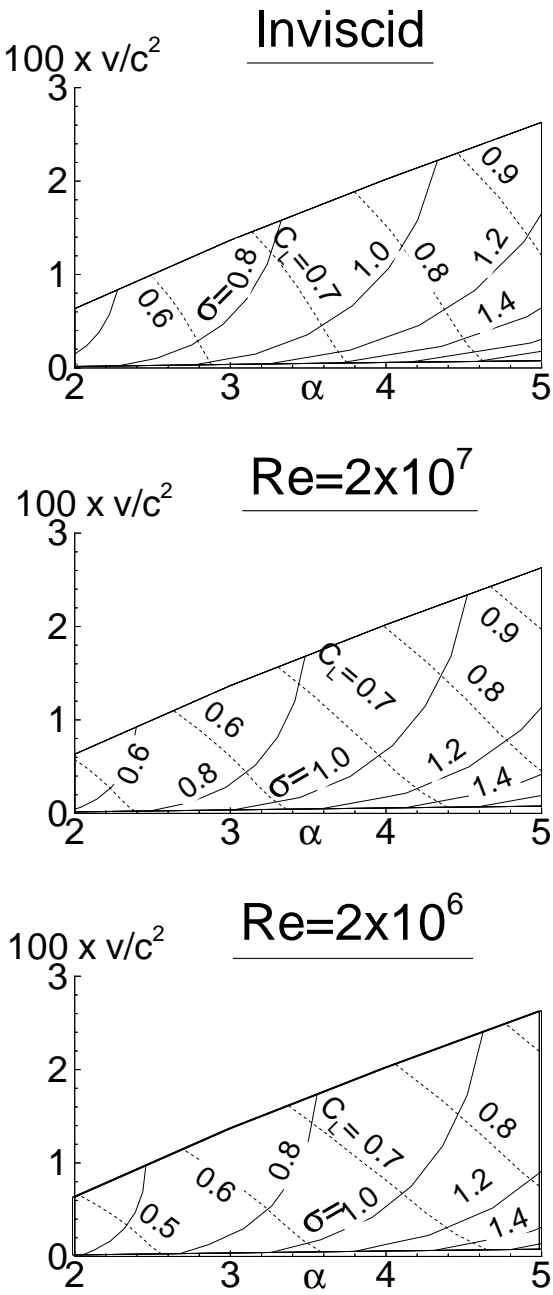


Figure 23: Contour plots of constant lift coefficient and cavitation number versus cavity volume and angle of attack. Predicted by the present method for inviscid flow (top), $Re = 2 \times 10^7$ (middle) and $Re = 2 \times 10^6$ (bottom); $NACA66(\tau/c = 0.07)$, $NACA a = 0.8(f_o/c = 0.02)$.

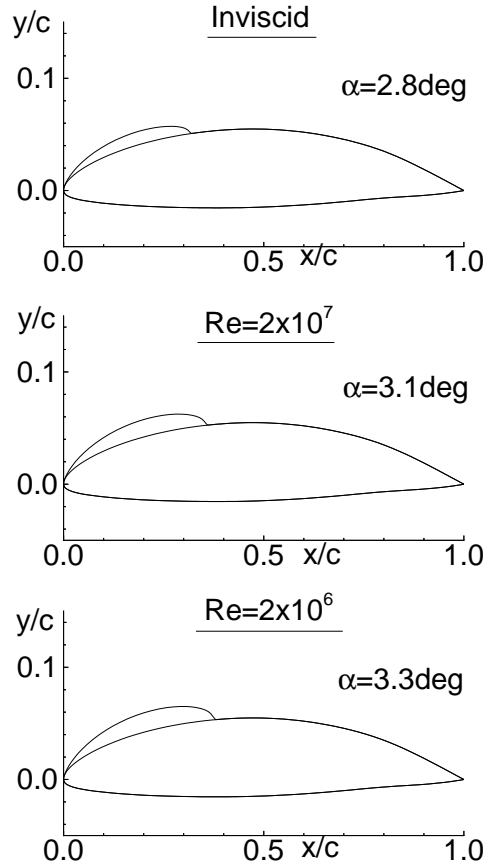


Figure 24: Cavity shapes predicted by the inviscid and the present viscous method for two Reynolds numbers. All hydrofoil sections are at $C_L = 0.6$ and $\sigma = 0.8$. The corresponding angles of attack are shown next to each foil. $NACA66(\tau/c = 0.07)$, $NACA a = 0.8(f_o/c = 0.02)$.

4.2 Super-Cavitating Hydrofoil

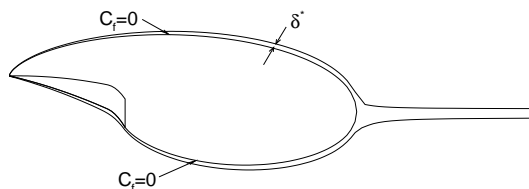


Figure 25: Super-cavitating hydrofoil with its boundary displacement thickness.

Consider a super-cavitating hydrofoil in viscous flow, as shown in Figure 25. In a similar manner, as in the case of partial cavitation, we first solve the inviscid cavity flow in non-linear theory [11]. We then apply the boundary layer equations on the compound foil, confined by the pressure side of the hydrofoil and the cavity boundary. A zero friction condition is applied everywhere on the cavity, as shown in Figure 25.

Results from applying this method are shown in Figure 26. The resulting boundary layer displacement thickness is shown at the top of the figure. The pressure distributions in inviscid and viscous flow are also shown. Notice that viscosity has a very small effect on the pressure distribution. The reader is reminded that this was not the case for partial cavitation, as may be seen in Figure 7. In other words, for super-cavitation, the cavitation number in viscous flow for given cavity length, l , is practically identical to that in inviscid flow. The friction coefficient, C_f , on the pressure side of the foil and cavity, is also shown at the bottom part of Figure 26.

The lift and drag on the hydrofoil are evaluated by integrating the pressure forces acting on all sides of the hydrofoil (the constant cavity pressure is applied on the cavitating sides of the hydrofoil) as well as the frictional forces acting on the wetted side of the hydrofoil. The convergence of the cavity solution and the predicted forces with number of panels is given on Table 3.

Finally the predicted σ , C_L , and C_D vs. l curves are shown in Figures 27 and 28, for a super-cavitating section at two angles of attack in inviscid flow and for two Reynolds numbers⁷. The super-cavitating section is a combination of a NACA 4digit camber form (with the maximum

⁷Based on l .

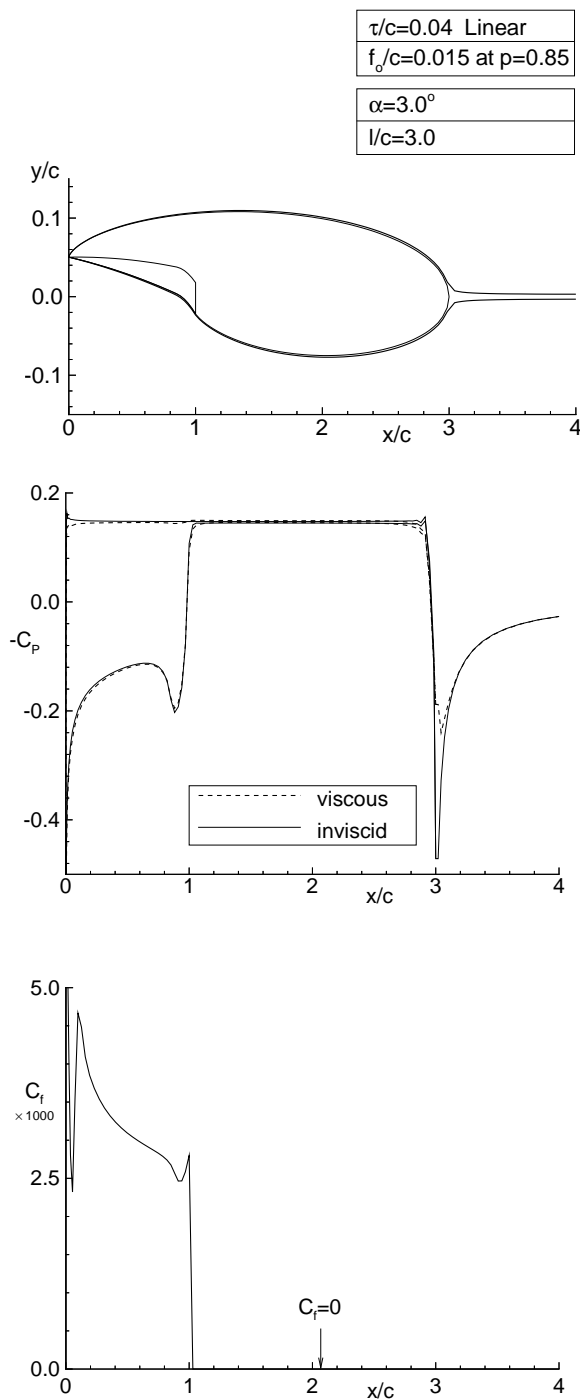


Figure 26: Super-cavitating hydrofoil in inviscid and viscous flow at $Re = 2 \times 10^7$. Cavity shape and boundary layer displacement thickness (top); pressure distributions (middle); and friction coefficient on the pressure side of the foil and cavity (bottom). All predicted by the present method.

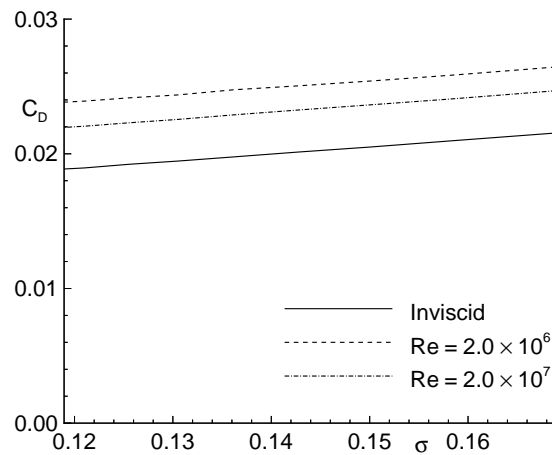
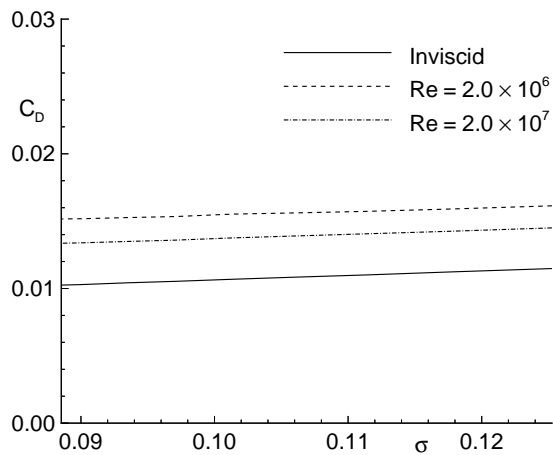
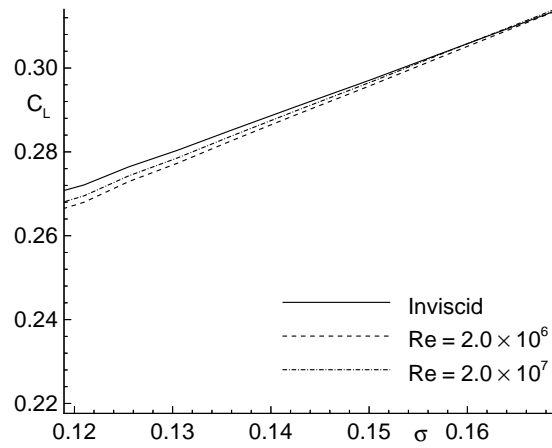
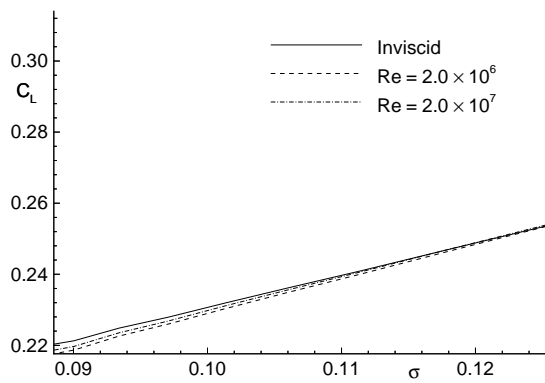
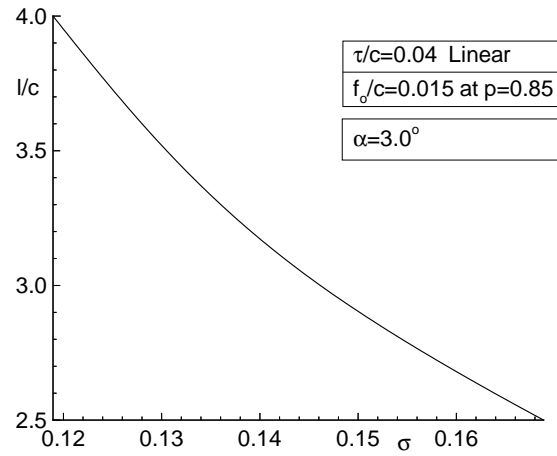
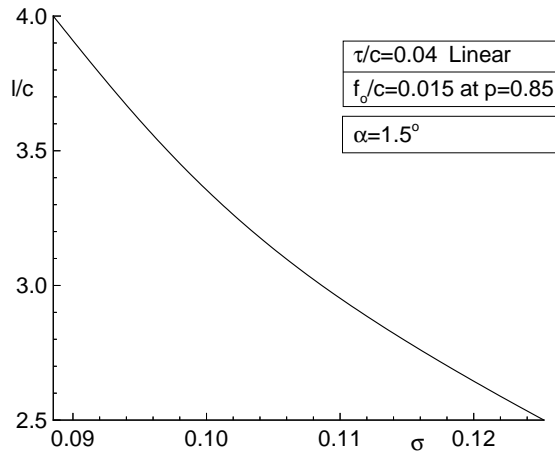


Figure 27: Cavity length, lift and drag coefficient versus cavitation number for a super-cavitating hydrofoil at $\alpha = 1.5^\circ$, in inviscid and viscous flow; predicted by the present method.

Figure 28: Cavity length, lift and drag coefficient versus cavitation number for a super-cavitating hydrofoil at $\alpha = 3^\circ$, in inviscid and viscous flow; predicted by the present method.

N	σ	V/c^2	C_L	C_D
100	0.145	0.365	0.282	0.0219
160	0.146	0.364	0.287	0.0223
200	0.146	0.363	0.292	0.0231

Table 3: Convergence of viscous cavity solution (σ , V/c^2 , C_L and C_D) with number of panels. Super-cavitating hydrofoil; $\tau/c = 0.045$, $f_o/c = 0.015$, $p = 0.85$, $\alpha = 3^\circ$.

camber f_o at $x = p$) and a linear thickness form. The effect of viscosity on lift coefficient is shown to be very small.

4.3 The “equivalent” σ

As already mentioned in Section 4.1, during the design of a hydrofoil or propeller the cavitation number and the lift (thrust) requirements must remain fixed. However, as was shown in Figures 20 to 23, inviscid theory would underpredict the extent and size of cavities. By using these figures, someone can find the “equivalent” σ in inviscid theory, which for the same lift coefficient would produce the same cavity volume (or length) as viscous theory for the given C_L and the original value of σ .

The equivalent σ , in the case of finite span hydrofoils or propellers, may be estimated by applying the 2-D theory on the local section geometry and lift coefficient at which the maximum extent of cavitation appears.

5 CONCLUSIONS

The viscous flow around cavitating hydrofoils was addressed by coupling an inviscid non-linear cavity model with a boundary layer solver. The cavity detachment point is set where laminar separation occurs just upstream of the cavity. In the case of partial cavitation, it was found that inviscid cavity theory: (a) overpredicts the cavity extent and volume for fixed cavitation number and angle of attack and, (b) underpredicts the cavity extent and volume for fixed cavitation number and lift coefficient. In the case of super-cavitation, the effect of viscosity on the predicted cavitation number for given cavity extent, was found to be negligible. The *equivalent* cavitation number was

introduced as a way of including the effects of viscosity in the case of cavitating flows in three dimensions.

Future efforts will include: (a) *systematic* validation of the results of the present method with experiments and, (b) direct application of the method in three dimensions.

6 ACKNOWLEDGEMENTS

Support for this research was provided by the Applied Hydromechanics Research program administered by the Office of Naval Research and by an MIT/ Navy/ Industry Consortium on High Speed Propulsors with the following members: DTMB, OMC, Mercury, Volvo-Penta, IHI, Daewoo, El Pardo MB, HSVA, KaMeWa, Propellum, Rolla, Sulzer-Escher Wyss, Hyundai and Wart-sila.

References

- [1] H. Arakeri. Viscous effects on the position of cavitation separation from smooth bodies. *Journal of Fluid Mechanics*, vol 68(No. 4):pp 779–799, 1975.
- [2] A.H. Armstrong. Abrupt and smooth separation in plane and axisymmetric flow. Technical Report No. 22/53, Mem. Arm. Res. Est., G.B., 1953.
- [3] M. Brillouin. Les surfaces de glissement de Helmholtz et la resistance des fluides. *Ann. Chim. Phys.*, vol. 23:pp. 145–230, 1911.
- [4] M. Drela. XFOIL: An analysis and design system for low Reynolds number airfoils. In *Lecture Notes in Engineering (Volume 54, Low Reynolds Number Aerodynamics)*, New York, 1989. Springer-Verlag.
- [5] N. E. Fine. *Nonlinear Analysis of Cavitating Propellers in Nonuniform Flow*. PhD thesis, Department of Ocean Engineering, MIT, October, 1992.
- [6] N.E. Fine and S.A. Kinnas. A boundary element method for the analysis of the flow around 3-d cavitating hydrofoils. *Journal of Ship Research*, 37:213–224, September 1993.
- [7] J.P. Franc and J.M. Michel. Attached cavitation and the boundary layer: Experimental investigation and numerical treatment. *Journal of Fluid Mechanics*, vol. 154:pp 63–90, 1985.

- [8] G.S. Hufford, M. Drela, and J.E. Kerwin. Viscous flow around marine propellers using boundary-layer strip theory. *Journal of Ship Research*, 38(1):pp. 52–62, March 1994.
- [9] J.E. Kerwin, S.A. Kinnas, J-T Lee, and W-Z Shih. A surface panel method for the hydrodynamic analysis of ducted propellers. *Trans. SNAME*, 95, 1987.
- [10] S.A. Kinnas and N.E. Fine. Analysis of the flow around supercavitating hydrofoils with midchord and face cavity detachment. *Journal of Ship Research*, 35(3):pp. 198–209, September 1991.
- [11] S.A. Kinnas and N.E. Fine. Non-Linear Analysis of the Flow Around Partially or Super-Cavitating Hydrofoils by a Potential Based Panel Method. In *Boundary Integral Methods-Theory and Applications, Proceedings of the IABEM-90 Symposium, Rome, Italy, October 15-19, 1990*, pages 289–300, Heidelberg, 1991. Springer-Verlag.
- [12] S.A. Kinnas and N.E. Fine. A nonlinear boundary element method for the analysis of unsteady propeller sheet cavitation. In *Proceedings of the Nineteenth Symposium on Naval Hydrodynamics*, pages 717–737, Seoul, Korea, August 1992.
- [13] S.A. Kinnas and N.E. Fine. A numerical nonlinear analysis of the flow around two- and three-dimensional partially cavitating hydrofoils. *Journal of Fluid Mechanics*, 254:151–181, September 1993.
- [14] J.-T. Lee. *A Potential Based Panel Method for The Analysis of Marine Propellers in Steady Flow*. PhD thesis, M.I.T., Department of Ocean Engineering, August 1987.
- [15] H. Lemonnier and A. Rowe. Another approach in modelling cavitating flows. *Journal of Fluid Mechanics*, vol 195, 1988.
- [16] L. Morino and C.-C. Kuo. Subsonic Potential Aerodynamic for Complex Configurations : A General Theory. *AIAA Journal*, vol 12(no 2):pp 191–197, February 1974.
- [17] H. Schlichting. *Boundary-Layer Theory*. McGraw-Hill, Inc., 1979.
- [18] H. Villat. Sur la validité des solutions de certain problem d’hydrodynamique. *J. de Math.*, vol 6(No. 10):pp 231–290, 1914.
- [19] R.A. Villeneuve. Effects of viscosity on hydrofoil cavitation. Master’s thesis, Massachusetts Institute of Technology, May 1993.
- [20] F.M. White. *Viscous Fluid Flow*. McGraw-Hill, Inc., 1974.

A The Blended Spacing

When employing the inviscid cavity model, already described in Section 2, a panel arrangement is desired in which: (a) the number of panels at the foil and cavity leading edge is *independent* of the total number of panels; (b) the cavity detachment point and the cavity end are panel boundaries and (c) there is smooth transition of the panel size in the vicinity of the cavity start and end. Originally [11], two cosine spacings were used between the foil leading edge and the cavity end and between the cavity end and the foil trailing edge. This arrangement (called double cosine spacing) though, does not satisfy *all* of the desired requirements. In the process of introducing a new spacing the following problem must be addressed first:

Define a sequence of N intervals, Δx_i ; $i = 1, \dots, N$, between $x = a$ and $x = b > a$ which “blends nicely” to given intervals at the two ends (Δx_1 and Δx_N). To accomplish this we first make the following definitions:

$$\overline{\Delta x} = \frac{b - a}{N} \quad (45)$$

$$f(i; N) = \frac{\Delta x_i}{\overline{\Delta x}} \quad (46)$$

$$A = \frac{\Delta x_1}{\overline{\Delta x}} \quad (47)$$

$$B = \frac{\Delta x_N}{\overline{\Delta x}} \quad (48)$$

The progression $f(i; N)$ must then satisfy the conditions:

$$f(1; N) = A \quad (49)$$

$$f(N; N) = B \quad (50)$$

$$\sum_1^N f(i; N) = N \quad (51)$$

We define the following progressions, both of which automatically satisfy conditions (49) and (50):

$$f(i; N) = A \frac{N - i}{N - 1} + B \frac{i - 1}{N - 1} + K_1 \frac{(N - i)(i - 1)}{(N - 1)^2} \quad (52)$$

$$f(i; N) = A \left(\frac{N-i}{N-1} \right)^2 + B \left(\frac{i-1}{N-1} \right)^2 + K_2 \frac{(N-i)^2(i-1)^2}{(N-1)^4} \quad (53)$$

The coefficients K_1 and K_2 are then determined from satisfying condition (51). It can be shown, after lengthy algebra, that:

$$K_1 = \frac{6(N-1)}{(N-2)} \left[1 - \frac{A+B}{2} \right], \quad (54)$$

and:

$$K_2 = \frac{30(N-1)^2}{(N^3 - 4N^2 + 6N - 4)} \times \left[N - 1 - \frac{2N-1}{6}(A+B) \right] \quad (55)$$

We call the blended spacings defined from equations (52) and (53) linear and parabolic, respectively⁸. For both spacings there is a critical number of panels, beyond which the method results into $f(i; N) < 0$, i.e. negative intervals.

The blended grid, in the case of partial cavitation, is then defined as follows⁹:

- for $0 < x < l_D$: N_{LE} panels with half-cosine spacing.
- for $l_D < x < l$: N_C panels with parabolic blended spacing; the left end interval is set equal to the right end interval of the previous spacing, and the right end interval is set equal to Δx_{TE}^C .
- for $l < x < 1$: N_{FW} panels with parabolic blended spacing; the left end interval is equal to Δx_{TE}^C and the right end interval is equal to Δx_{TE}^{FW} .

Where $N_H = N/2$, $N_C = N_H \times l - N_{LE}$ and $N_{FW} = N_H - N_C - N_{LE}$ with N being the total number of panels. N_{LE} is defined from:

$$N_{LE} = N_R \left(\frac{l_D}{\rho_{LE}} \right)^{\frac{1}{2}} \quad (56)$$

with N_R being a fixed number of panels for $0 < x < \rho_{LE}$ with ρ_{LE} being the leading edge radius. In our current spacing we have selected: $N_R = 3$ and $\Delta x_{TE}^C = \Delta x_{TE}^{FW} = 1/N_H$.

⁸They become linear and quadratic functions of i for $K_1 = 0$ and $K_2 = 0$.

⁹The given number of panels refers to each side of the foil.

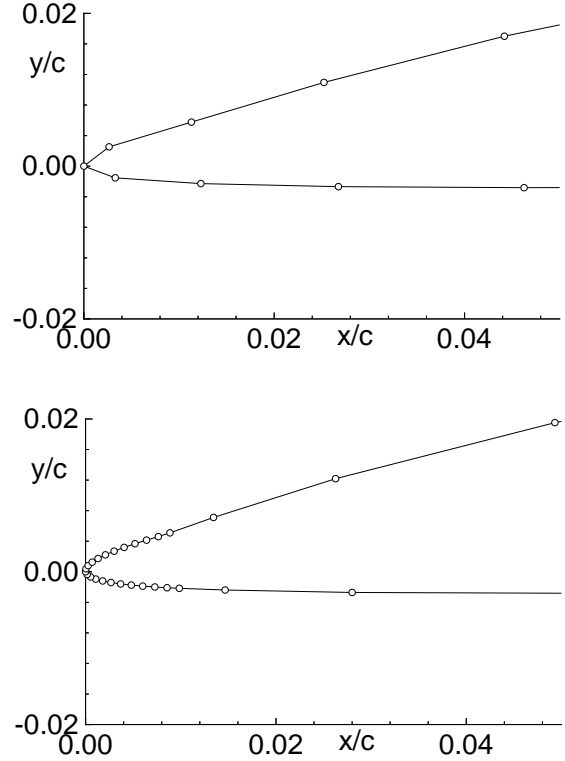


Figure 29: Arrangement of panels at the leading edge of a partially cavitating hydrofoil. Double cosine spacing (top) and blended spacing (bottom). The total number of panels is equal to 100 in both cases.

The panel arrangements in the vicinity of the leading edge, resulting from the original double cosine and the proposed blended spacing, are shown in Figure 29. Notice the finer resolution in the case of the blended spacing.

The convergence of the results with number of panels, from applying the inviscid cavity model on the two grids is shown in Figures 30 and 31. Notice that the cavity solution and the foil forces converge faster when the blended grid is employed. The improvement of the convergence by using the blended grid appears to be more pronounced in the calculation of drag, as expected, due to the higher panel resolution at the leading edge. The blended spacing has been found to improve the convergence of the presented viscous cavity model as well.

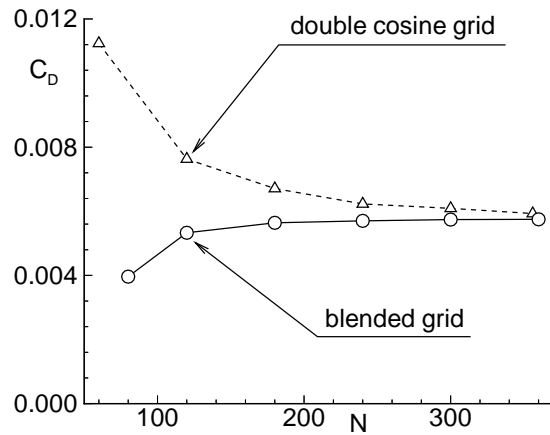
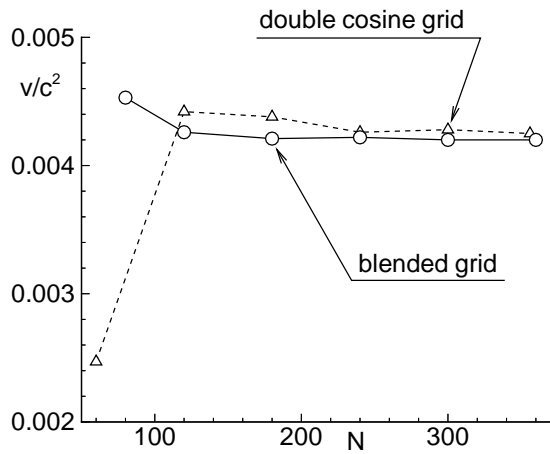
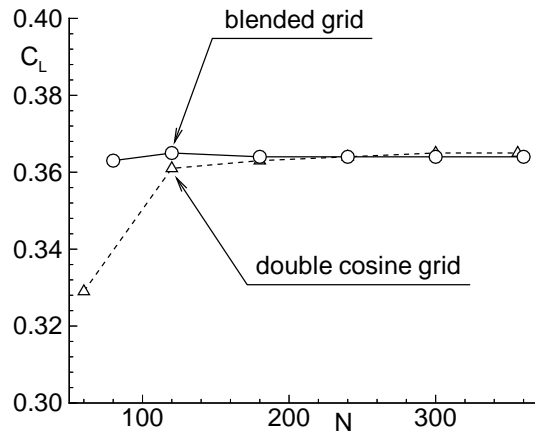
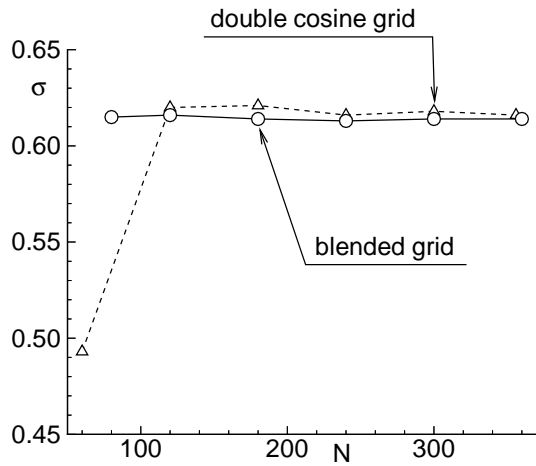


Figure 30: Convergence of the cavity solution predicted by the present method for two different panel arrangements; $\tau/c = 0.04$, $f_o/c = 0.02$, $\alpha = 3^\circ$, $l/c = 0.35$, $l_D/c = 0.008$.

Figure 31: Convergence of the forces predicted by the present method for two different panel arrangements; same hydrofoil geometry as in the previous figure.